inorganics

MDPI

Article

Ce–Metal–Organic Framework-Derived CeO_2–GO: An Efficient Electrocatalyst for Oxygen Evolution Reaction

Patnamsetty Chidanandha Nagajyothi [1], Krishnapuram Pavani [2], Rajavaram Ramaraghavulu [3] and Jaesool Shim [1,*]

[1] School of Mechanical Engineering, Yeungnam University, Gyeongsan 38541, Republic of Korea
[2] I3N—Department of Physics, University of Aveiro, 3810-193 Aveiro, Portugal
[3] Department of Physics, School of Applied Science, REVA University, Bangalore 560064, India
* Correspondence: jshim@ynu.ac.kr

Abstract: The oxygen evolution reaction (OER) is a crucial half-reaction in water splitting. However, this reaction is kinetically sluggish owing to the four-electron (4 e^-) transfer process. Therefore, the development of low-cost, stable, highly efficient, and earth-abundant electrocatalysts for the OER is highly desirable. Metal oxides derived from metal–organic frameworks (MOFs) are among the most efficient electrocatalysts for the OER. Herein, Ce–MOF-derived CeO_2/graphene oxide (GO) composites were successfully prepared using a facile method. The composites with 0, 25, 50, and 100 mg GO were named CeO_2, CeO_2–GO-1, CeO_2–GO-2, and CeO_2–GO-3, respectively. The physicochemical characteristics of the electrocatalysts were assessed using several analytical techniques, including X-ray diffraction (XRD), scanning electron microscopy (SEM), high-resolution transmission electron microscopy (HR-TEM), X-ray photoelectron spectroscopy (XPS), and Brunauer–Emmett–Teller (BET) analysis. The TEM results revealed that the CeO_2 had a sheet-like morphology and that a GO layer was noticeable in the synthesized CeO_2–GO-3 composite. The characterization results confirmed the formation of impurity-free CeO_2–GO composites. The OER activity and stability were measured using cyclic voltammetry (CV), linear sweep voltammetry (LSV), chronoamperometry (CA), and electrochemical impedance spectroscopy (EIS). The CeO_2–GO-3 electrocatalyst has a smaller Tafel slope (176 mV·dec^{-1}) and lower overpotential (240 mV) than the other electrocatalysts. In addition, it exhibited high cyclic stability for up to 10 h. Therefore, the inexpensive CeO_2–GO-3 electrocatalyst is a promising OER candidate.

Keywords: cerium oxide–graphene oxide composite; room-temperature synthesis; electrocatalyst; oxygen evolution reaction

Citation: Nagajyothi, P.C.; Pavani, K.; Ramaraghavulu, R.; Shim, J. Ce–Metal–Organic Framework-Derived CeO_2–GO: An Efficient Electrocatalyst for Oxygen Evolution Reaction. *Inorganics* **2023**, *11*, 161. https://doi.org/10.3390/inorganics11040161

Academic Editors: Zuzana Vlckova Zivcova and Francis Verpoort

Received: 15 December 2022
Revised: 24 March 2023
Accepted: 4 April 2023
Published: 11 April 2023

1. Introduction

Electrochemical water splitting is a promising method for producing pollution-free, clean hydrogen [1]. Water electrolysis consists of two half-reactions (OER and HER): the oxygen evolution reaction at the anode and the hydrogen (H_2) evolution reaction at the cathode [2]. However, the OER is kinetically slow owing to its four-electron transfer process [3]. Therefore, highly effective and reliable OER electrocatalysts must be developed to address this limitation. Noble metal oxide catalysts, such as RuO_2 and IrO_2, are among the most efficient electrocatalysts for OER activity; however, their high prices and scarcity limit their large-scale application [4]. Therefore, the development of OER electrocatalysts with high activity, long-term stability, and low cost is essential.

Metal-organic frameworks (MOFs) are a new class of porous materials composed of metal ions or clusters connected to organic ligands via coordination bonds to form one-dimensional, two-dimensional, and three-dimensional (1D, 2D, and 3D) structures [5]. Recently, MOFs have emerged as promising candidates for energy- and environment-related applications [6,7] owing to their unique characteristics, such as high porosity, high

specific surface areas, good thermal stability, and ease of modification [8,9]. However, the poor electrical conductivity of pure MOFs limits their use in electrochemistry applications [10]. To overcome these limitations, the conversion of MOFs (MOFs as precursors or templates) into metal oxides, porous carbon materials, metal hydroxides [11], metal phosphides [12], metal sulfides [13], selenides [14], or their composites [11,15] has been widely investigated for electrochemical applications.

MOF-derived materials exhibit unique properties, such as tailorable morphologies, hierarchical porous structures, chemical and structural stabilities, high electrical conductivity, and simple surface functionalization [16]. Moreover, they play significant roles in various energy-related applications, such as lithium-ion batteries [17], OER [18], methanol oxidation reactions [19], urea oxidation reactions [20], fuel cells [21], and HER [22]. Gao Han et al. [23] synthesized a bimetal oxide $CuCoO_2$ using ZIF-67 and Cu-BTC (Co and Cu sources) through a single-step solvothermal procedure. The synthesized $CuCoO_2$ was used as an electrocatalyst for the OER. With a low overpotential, a smaller Tafel slope, and good durability in a 1.0 M KOH solution, the synthesized $CuCoO_2$ exhibited higher OER activity.

Cerium oxide, also known as ceria (CeO_2), has drawn considerable attention owing to its low cost, non-toxicity, earth-abundance, and tunable oxygen vacancies via a reversible transition between the Ce^{3+} and Ce^{4+} oxidation states, and high oxygen (O_2) storage capacity [24,25]. These properties make CeO_2 a promising material for various applications, such as photocatalytic, forensic, electrochemical [26], and humidity sensors [27], as well as catalytic oxidation [28], supercapacitors [29], and biological [30] applications. However, pure CeO_2 exhibits limited OER/ORR performance owing to its weak electronic conductivity [25,31]. The best method to improve the dispersibility and conductivity of CeO_2 is through deposition on conducting carbon-based materials [31].

Graphene oxide (GO) is the oxidized form of graphene with a layered structure and shows good mechanical, electrical, and thermal properties due to its structural and morphological characteristics [32,33]. GO structures comprise oxygen-based functional groups, such as hydroxyl (–OH), carboxyl (–COOH), epoxide (C–O–C), and carbonyl (C=O), that enable the dispersibility of the material in water [33,34]. In addition, as these oxygenated functional groups are chemically active, GO can be decorated with a variety of materials [35], such as metals, metal oxides, ZIFs, MOFs, and MOF-derived metal oxides. GO-based composites have a high potential for various applications in energy- and environment-related fields, including dye removal (GO/SiO_2NH_2) [36], heavy metal removal (TiO_2/GO) [32], photochemical degradation of toluene (GO-TiO_2) [37], proton exchange membrane fuel cell (CeO_2–GO) [38], supercapacitors (GO, GO–CuO, and GO–ZnO) [39], OER (CeO_2/Cu–MOF/GO) [40], HER (Pd@GO/MOF) [41], OER, ORR, and Zn–air batteries (ZnCo–ZIF@GO) [42]. Malik et al. [43] synthesized CeO_2 from a GO@Ce–MOF precursor and used it as an electrocatalyst for OER applications. According to Dongyang et al. [44], a simple chemical co-precipitation process was used to produce CeO_2 nanoparticles decorated on GO. CeO_2/GO is used as an electrode material in supercapacitor applications; the CeO_2/GO electrode demonstrated exceptional supercapacitive behavior with high specific capacitance. Kasinath and Byrappa [45] synthesized hexagonal CeO_2@nitrogen-doped GO composites for OER and ORR studies. The CeO_2/NGO composites revealed a high anodic onset potential for ORR and OER activity (0.925 V vs. RHE for ORR and 1.2 V for OER) with a high current density in 0.5 M KOH.

In this study, we successfully synthesized Ce–MOF-derived CeO_2–GO composites using a simple, room-temperature synthesis method followed by annealing at 400 °C in the air for 1 h. The as-synthesized composites were used as electrocatalysts for the OER. Compared with the CeO_2–GO-1 and CeO_2–GO-2 composites, the CeO_2–GO-3 electrocatalyst exhibited higher OER activity and stability. The synthetic process is illustrated in Scheme 1.

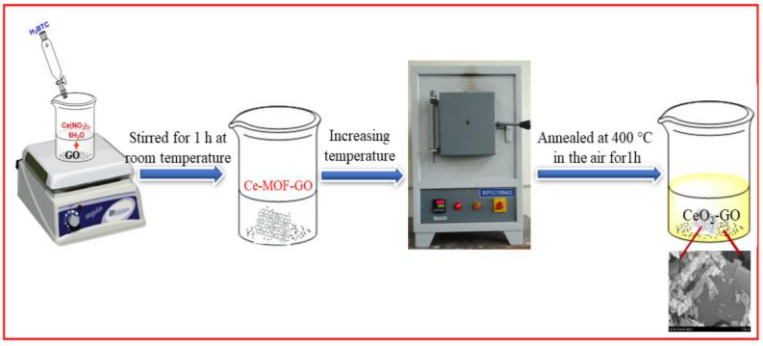

Scheme 1. Schematic of the synthesis of the CeO_2–GO-3 electrocatalyst.

2. Results and Discussion

2.1. Characterization of the Electrocatalysts

Figure 1a displays the X-ray diffraction (XRD) patterns of the pristine CeO_2 and CeO_2–GO electrocatalysts. The XRD data of Ce–MOF, as shown in Figure S1, exhibit sharp and narrow peaks. All diffraction peaks matched the XRD patterns of previous reports [46,47]. After calcination, the Ce–MOF was fully converted into cubic-structured CeO_2. The four characteristic peaks at 28.4°, 33.1°, 47.3°, and 56.3° can be attributed to the (111), (200), (220), and (311) planes (Figure 1a) [48], which are in good agreement with JCPDS 00-004-0593. The average crystallite size was found using the Debye–Scherrer equation [49],

$$D = \frac{k\lambda}{\beta\, cos\theta} \tag{1}$$

where D is the average crystallite size (nm), k is constant (0.9), λ is the wavelength of X-ray radiation (1.5416 Å), θ is diffraction angle, and β is the full-width half maxima of diffraction peaks. From XRD data, the average size was found to be in the range of 10 to 15 nm. The calculated lattice parameters and volume were found to be (for pure cubic structure a = b = c; $\alpha = \beta = \gamma = 90°$) a = 1.5411 Å and V = 161.05 $Å^3$. Malik et al. [43] reported similar results for CeO_2 derived from the GO–Ce–MOF. A GO peak in the CeO_2–GO electrocatalysts was noted at 10.8° (001), indicating the presence of GO in all synthesized samples [50]. Compared with CeO_2–GO-1 and CeO_2–GO-2, the CeO_2–GO-3 electrocatalyst showed the peak (10.8°) intensity, increasing with an increase in graphene oxide.

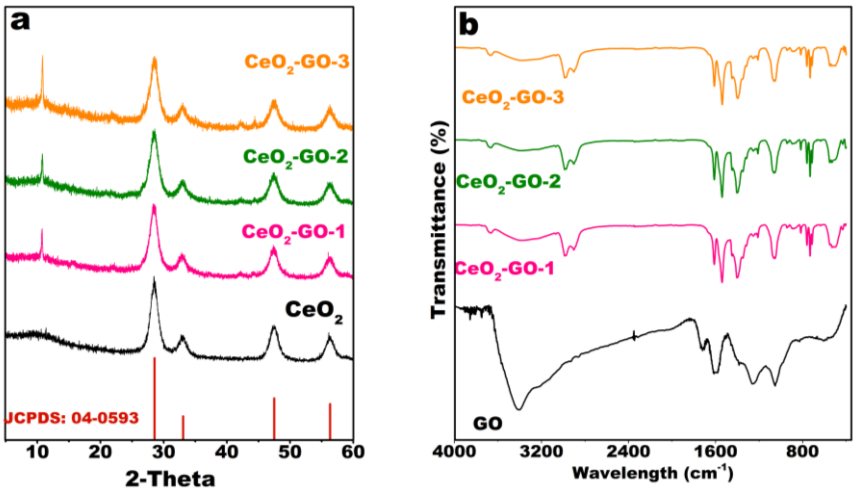

Figure 1. (**a**) XRD pattern and (**b**) FT−IR spectra of the electrocatalysts.

The Fourier-transform infrared spectra (FTIR) of the pure CeO_2 and CeO_2–GO electrocatalysts are presented in Figure 1b. The FTIR spectrum of GO exhibits a prominent

peak at 3409 cm^{-1}, which is attributed to the O–H stretching; further absorption peaks at 1717, 1606, 1258, and 1051 cm^{-1} correspond to the C=O stretching vibrations, C=C, C–O–C bending, and C–O stretching groups [51–53], respectively. A Ce–O stretching vibration was observed in the CeO_2–GO composites at 535 cm^{-1} [43,54]. The bands at 1621 and 1059 cm^{-1} are related to the bending vibration of the hydroxyl (–OH) groups of water molecules [55] and Ce–O–Ce stretching vibration [56], respectively. Most of the GO peaks were significantly reduced after the CeO_2–GO composite formation.

The surface chemical states of the Ce–MOF-derived CeO_2 and CeO_2–GO-3 electrocatalysts were studied using X-ray photoelectron spectroscopy (XPS; Figure 2a). A survey scan revealed the presence of Ce 3d, O 1s, and C 1s in the electrocatalysts. The Ce 3d spectra of the CeO_2 and CeO_2–GO-3 electrocatalysts were fitted to eight peaks: the Ce $3d_{3/2}$ peaks at 900.1/900.3, 906.7/906.8, and 916.0/916.1 eV; Ce $3d_{5/2}$ peaks at 881.6/881.8, 887.9/888.0, and 897.5/897.6 eV, which are associated with Ce^{4+}; and peaks at 884.6/884.8 eV (Ce $3d_{5/2}$) and 903.1/903.3 eV (Ce $3d_{3/2}$) associated with Ce^{3+} (Figure 2c). These values are consistent with those reported in the literature [57–59]. The deconvolution of the O 1s spectra displayed two peaks at 528.6/528.8 and 531.0/531.1 eV (Figure 2b), which are attributed to the lattice and adsorbed oxygen [60,61]. In the composite, the C 1s spectrum (Figure 2d) peaks at 284.5/284.4, 285.8/286.1, 288.4/288.1, and 289.5 eV are ascribed to the C=C, C-O bonds, carbonyl (C=O), and carboxyl (HO–C=O) bonds [62–64], respectively. The 289.5 eV small peak vanished in the CeO_2 electrocatalyst but was clearly visible in the CeO_2–GO-3 electrocatalyst.

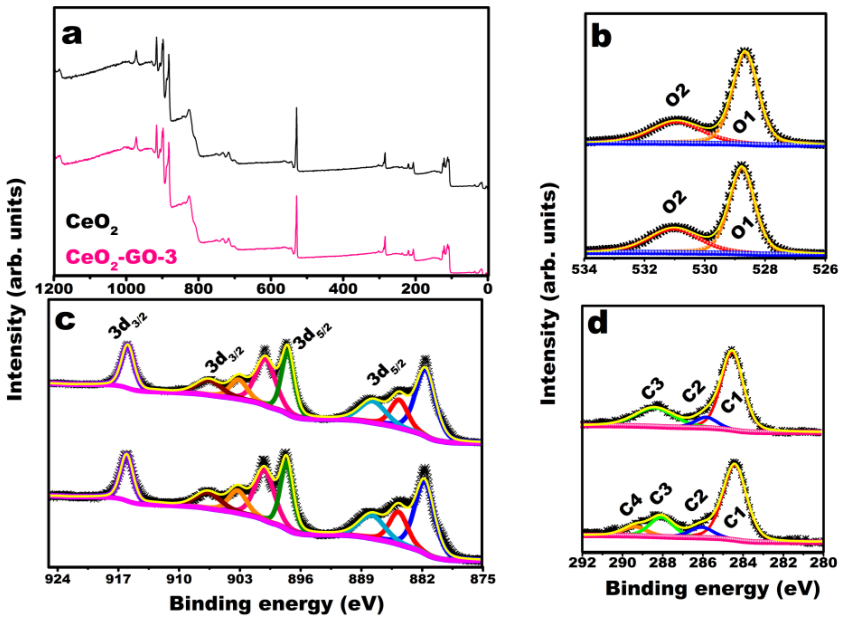

Figure 2. XPS analysis of the CeO_2 (**top view**) and CeO_2–GO-3 (**bottom view**) electrocatalysts: (**a**) survey scans, (**b**) O 1s, (**c**) Ce 3d, and (**d**) C 1s.

The morphologies of the Ce–MOF-derived CeO_2 and CeO_2–GO electrocatalysts were characterized via scanning electron microscopy (SEM; Figure 3). The CeO_2 sample had a rod-like morphology with the appearance of some merging rods having sheet-like structures (Figure 3a-1,a-2). Kohantorabi and Gholami [65] and Ye et al. [66] reported similar morphologies using benzene-1,3,5-tricarboxylic acid, and cerium nitrate hexahydrate, respectively. CeO_2 rods were visible in CeO_2–GO-1 and a few GO sheets were observed. The rods were uniformly spread on the GO sheets (Figure 3b-1,b-2). As the GO weight was increased, layered GO sheets with smooth surfaces were observed in the CeO_2–GO-2 and CeO_2–GO-3 samples (Figure 3c-1–d-2). These results confirmed the successful decoration of CeO_2 on the GO sheets.

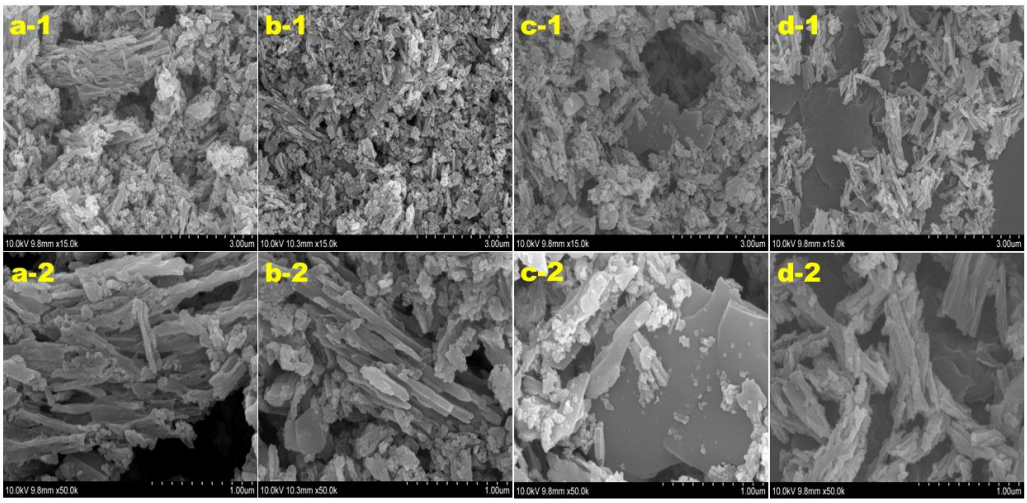

Figure 3. SEM analysis of the electrocatalysts; low and higher magnification of: (**a-1**,**a-2**) CeO_2, (**b-1**,**b-2**) CeO_2–GO-1, (**c-1**,**c-2**) CeO_2–GO-2, and (**d-1**,**d-2**) CeO_2–GO-3.

Energy-dispersive X-ray spectroscopy (EDS) was performed to identify the elements in the electrocatalyst, and the corresponding results are shown in Figure S2. The EDS spectrum validated the presence of O, Ce, and C in the electrocatalyst. Figure 4a,b shows the TEM images of the CeO_2–GO-3 electrocatalyst. The synthesized CeO_2 was confirmed to have a sheet-like morphology in the TEM images, and a GO layer was visible in the synthesized composites. The HR-TEM images (Figures 4c and S3–S5) showed a fringe spacing of 0.311, 0.315, and 0.163 nm, which is consistent with the d-spacing of the (111), (111), and (311) planes of CeO_2. The corresponding selected area electron diffraction (SAED) pattern displayed the polycrystalline nature of the synthesized catalyst (Figure 4d). The ring pattern of the SAED results suggests a similar plane ((111), (222), and (311)); therefore, the electrocatalyst matched well with the XRD results.

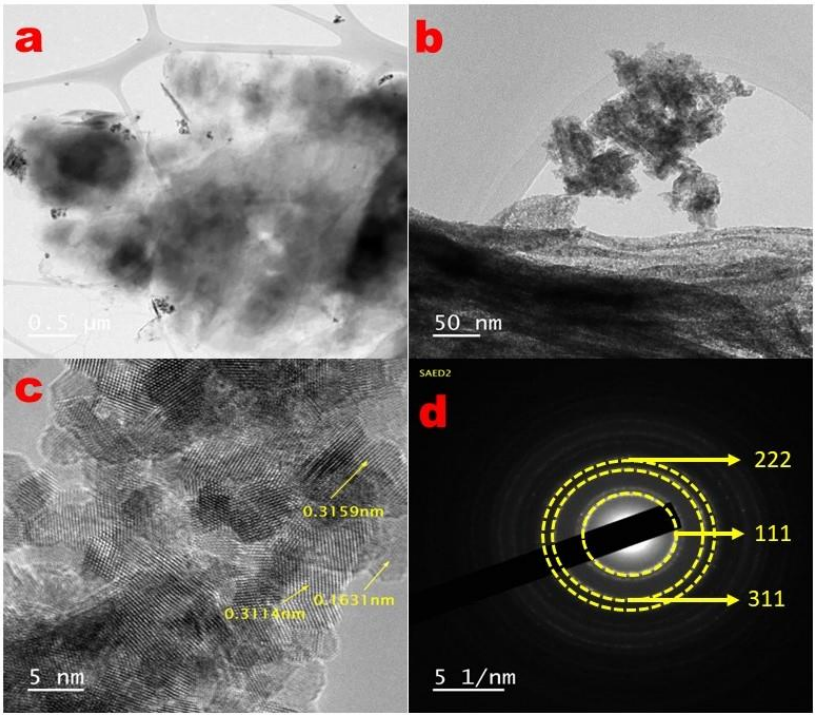

Figure 4. TEM images of the CeO_2–GO-3 electrocatalyst at (**a**) low and (**b**) high resolutions; (**c**) HR-TEM; and (**d**) SAED pattern.

2.2. OER Activity

We further explored the OER activity of the synthesized electrocatalysts under alkaline conditions. Figure 5 shows the cyclic voltammetry (CV) curves of the CeO_2, CeO_2–GO-1, CeO_2–GO-2, and CeO_2–GO-3 electrocatalysts under the three-electrode setup at room temperature. The CV curves were measured at a constant potential between 0.1~0.6 V against Hg/HgO at various scan rates (5–100 mVs^{-1}). These CV curves revealed that the current density increased with increasing GO content in the electrocatalyst owing to the increase in ion transport between the electrocatalyst (CeO_2) and GO (CeO_2–GO-3). Similarly, cerium oxide/reduced GO nanocomposites exhibited excellent photocatalytic and supercapacitor activities owing to the increased charge transport between the electrocatalysts [67,68]. Additionally, CeO_2/multi-walled carbon nanotube nanocomposites have higher capacitive performance and long-term stability [69], and the electrocatalytic performance increased after the introduction of carbon-based materials. Comparative CV curves of the electrocatalysts at a standard scan rate (60 mV s^{-1}) are shown in Figure S6. All electrocatalysts exhibited cathodic peaks at approximately 0.472, 0.502, 0.489, and 0.514 V and anodic peaks at approximately 0.304, 0.303, 0.301, and 0.296 V for CeO_2, CeO_2–GO-1, CeO_2–GO-2, and CeO_2–GO-3, respectively. These CV curves reveal that CeO_2–GO-3 exhibits a larger integral area, suggesting its higher electrochemical performance. The CV curves retained faradaic peaks even at higher scan rates, indicating a fast charge transport in the electrode system.

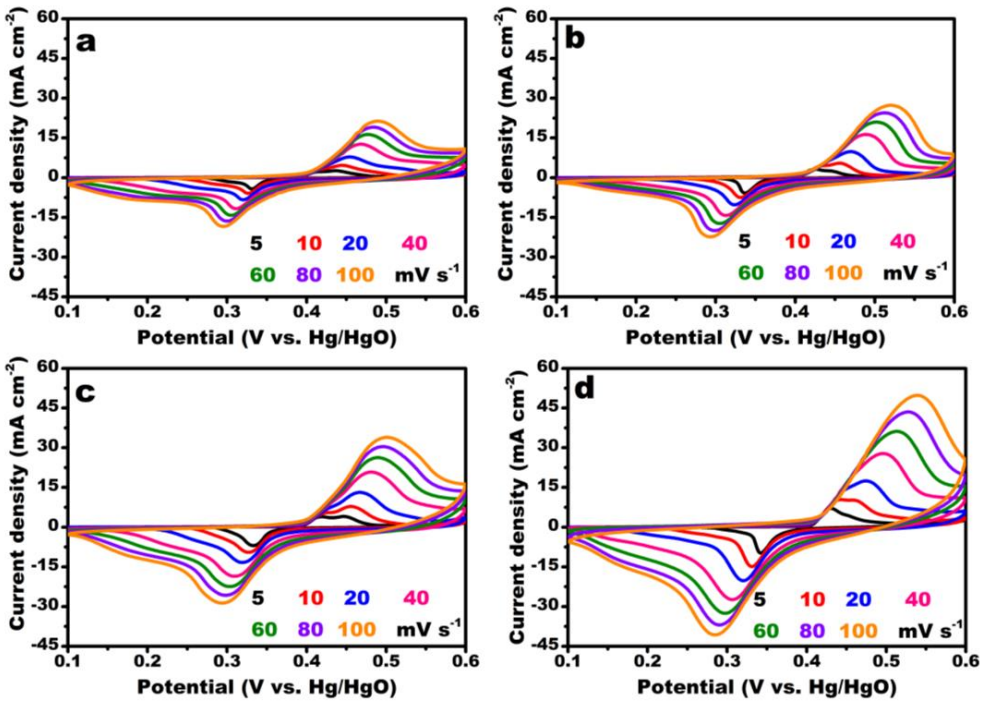

Figure 5. CV curves of the electrocatalysts in 1.0 M KOH at various scan rates for (**a**) CeO_2, (**b**) CeO_2–GO-1, (**c**) CeO_2–GO-2, and (**d**) CeO_2–GO-3.

The electrochemical OER activity was measured in the same electrolyte using linear sweep voltammetry (LSV), as revealed in Figure 6a. However, the GO content, which increased the OER performance, also increased, and the CeO_2–GO-3 electrocatalyst showed a higher current density at higher potentials. The overpotential decreased with increasing GO content in the electrocatalysts. The overpotentials of the CeO_2, CeO_2–GO-1, CeO_2–GO-2, CeO_2–GO-3, and RuO_2 electrocatalysts were 420, 360, 300, and 240, and 230 mV, respectively, at a fixed current density of 10 mA cm^{-2}. Among the electrocatalysts, CeO_2–GO-3 exhibited a lower overpotential; however, compared with standard RuO_2, there was not much difference. The electrocatalytic activity trend during the OER process followed the order CeO_2–GO-3 > CeO_2–GO-2 > CeO_2–GO-1 > CeO_2.

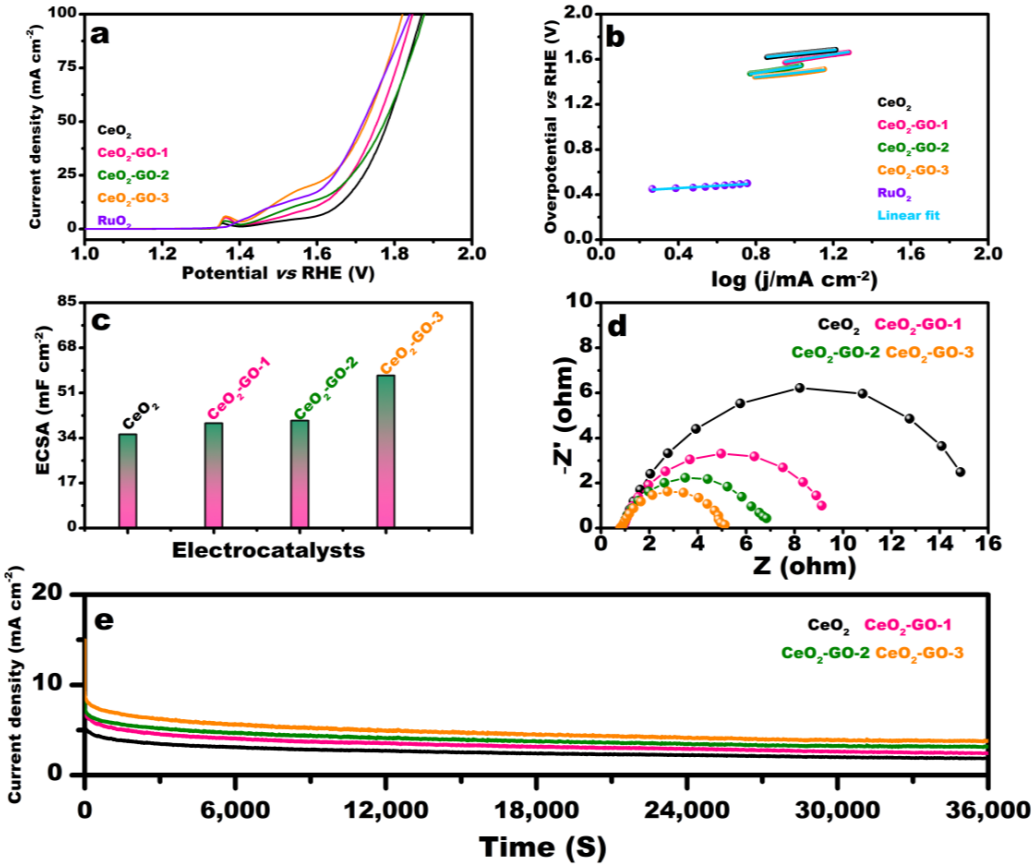

Figure 6. Electrochemical investigation of the electrocatalysts: (**a**) LSV curves, (**b**) Tafel slope, (**c**) bar diagram of the ECSA values, (**d**) Nyquist plots, and (**e**) chronoamperometry curves.

The Tafel slope is a crucial parameter for identifying the relationship between the overpotential and steady-state current density of electrocatalysts [66]. Figure 6b shows Tafel slopes of 261, 293, 185, 176, and 101 mV dec^{-1} for CeO_2, CeO_2–GO-1, CeO_2–GO-2, CeO_2–GO-3, and RuO_2 electrocatalysts, respectively. The CeO_2–GO-3 electrocatalyst revealed a smaller Tafel slope than the other electrocatalysts, showing its higher OER activity owing to the higher percentage of GO. However, compared with RuO_2, the CeO_2–GO-3 Tafel slope value was higher. The electrochemical active surface area (ECSA) is directly related to the electrochemical performance of the electrocatalysts [69,70]. A higher ECSA indicates better electrochemical performance. In the present work, the ECSA was measured using the CV curves in the non-faradaic region; the corresponding CVs are shown in Figure S7. The CeO_2–GO-3 electrocatalyst showed a higher ECSA (57.5 mF cm^{-2}) than the other electrocatalysts (35.4, 39.4, and 40.5 mF cm^{-2} for CeO_2, CeO_2–GO-1, and CeO_2–GO-2, respectively), as shown in Figure 6c.

Electrochemical impedance spectroscopy (EIS) was used to analyze the electrochemical dynamics of the electrocatalysts. Figure 6d and Table S1 show the EIS analysis of the electrocatalysts. The CeO_2–GO-3 electrocatalyst exhibited a smaller R_{ct} than the other electrocatalysts, revealing its lower charge transfer resistance owing to the increased electron transfer rate. The stability of electrocatalysts is a crucial parameter for OER activity. Therefore, chronoamperometry (CA) was used for the room-temperature analysis for approximately 10 h. Figure 6e depicts the CA curves of the electrocatalysts in a 1.0 M KOH solution, where the CeO_2–GO-3 electrocatalysts show a higher current density than the other electrocatalysts. Additionally, we compared our as-prepared materials to previously published OER electrocatalysts, which are depicted in Table S2.

The surface area plays a key role in electrochemical studies. In the present work, the surface area was measured via two different methods: the Brunauer–Emmett–Teller

(BET) method using nitrogen (N_2) gas adsorption and desorption and ECSA using the CV curves in the non-faradaic region of the electrocatalysts. Figure S8 shows the adsorption and desorption curves of the electrocatalysts. According to the IUPAC classification, these curves exhibit Type IV isotherms; all electrocatalysts showed similar type IV isotherms, which can be observed in mesoporous materials with a pore size of 2–50 nm [71]. The CeO_2–GO-3 electrocatalyst exhibited a higher BET surface area compared with the other electrocatalysts. In particular, the BET surface values for CeO_2, CeO_2–GO-1, CeO_2–GO-2, and CeO_2–GO-3 were 61.58, 80.77, 101.48, and 110.35 $m^2\ g^{-1}$, respectively. The pore volume and size of the CeO_2–GO-3 electrocatalyst were higher than those of the other electrocatalysts. These values are tabulated in the inset of Figure S8. Therefore, the electrocatalyst with a higher surface area exhibits higher electrocatalytic performance. In the present study, the CeO_2–GO-3 electrocatalyst showed a higher surface area and better electrocatalytic performance compared with the other electrocatalysts.

3. Materials and Methods

Ce–MOFs were synthesized using a previously reported method with slight modifications [46]. The required quantity of cerium nitrate hexahydrate (50.0 mM) was dissolved in a mixture of deionized water (DI) and ethanol (v/v of 1:1). Subsequently, trimesic acid (50.0 mM) was added to the milk-white suspension, which was stirred for 1 h at room temperature (RT). Thereafter, the temperature was increased until the solution evaporated. After cooling, the residue was collected and annealed at 400 °C in the air for 1 h to obtain the CeO_2 pure phase. The CeO_2–GO composites were prepared in the same manner with different GO contents (0, 25, 50, and 100 mg GO, denoted as CeO_2, CeO_2–GO-1, CeO_2–GO-2, and CeO_2–GO-3, respectively), as shown in Scheme 1. The chemicals, characterization, electrode preparation, and electrocatalytic performance followed are provided in the Supplementary Information (SI).

4. Conclusions

In this study, we successfully synthesized Ce–MOF-derived CeO_2 and CeO_2–GO electrocatalysts for the OER. The morphological and structural properties of the electrocatalysts were characterized. The TEM results indicated that the CeO_2–GO-3 electrocatalyst had a sheet-like morphology with an effective attachment to the GO sheets. The electrocatalysts produced using a low-cost, stable, and simple synthesis method demonstrated good OER activity in the 1.0 M KOH electrolyte. The CeO_2–GO-3 electrocatalyst had a low overpotential of 240 mV at 10 $mA{\cdot}cm^{-2}$ and a smaller Tafel slope (176 $mV{\cdot}dec^{-1}$) than the CeO_2–GO-1 and CeO_2–GO-2 electrocatalysts. Moreover, the CeO_2–GO-3 electrocatalyst exhibited considerable electrochemical stability over 10 h under alkaline conditions. Thus, this study provides a new method for developing non-noble-metal-based electrocatalysts for clean energy production.

Supplementary Materials: The following supporting information can be downloaded at https://www.mdpi.com/article/10.3390/inorganics11040161/s1: Figure S1: XRD pattern of the pristine Ce–MOF; Figure S2: EDS analysis of CeO_2–GO-3 electrocatalyst; Figure S3: d-spacing line profiles corresponding to the 0.311 (111) plane; Figure S4: d-spacing line profiles corresponding to the 0.315 (111) plane; Figure S5: d-spacing line profiles corresponding to the 0.163 (311) plane; Figure S6: Comparative CV curves at standard scan rate in aqueous 1.0 M KOH electrolyte; Figure S7: CV curves of the electrocatalysts in (a) 1.0 M KOH; CeO_2, (b) CeO_2–GO-1, (c) CeO_2–GO-2, and d) CeO_2–GO-3; Figure S8: N_2adsorption–desorption profiles of CeO_2, CeO_2–GO-1, CeO_2–GO-2, and CeO_2–GO-3; Table S1: EIS fitted values and the equivalent circuit; Table S2: Comparison of OER performance of different electrocatalysts [43,72–81].

Author Contributions: P.C.N.: synthesis, characterization, and application study, K.P.: investigation and conceptualization, R.R.: investigation and writing—original draft, J.S.: resources and funding acquisition. All authors have read and agreed to the published version of the manuscript.

Funding: This research was funded by the National Research Foundation of Korea (NRF) grants funded by the Korean government, grant numbers 2020R1A4A1019227 and 2020R1A2C1012439; and the National Funds (OE) through FCT, Portugal, I.P., in the scope of the framework contract foreseen in numbers 4, 5, and 6 of Article 23 of the Decree-Law 57/2016, of 29 August, changed by Law 57/2017, of 19 July and also within the scope of the project i3N, UIDB/50025/2020 and UIDP/50025/2020, financed by national funds through the FCT/MEC.

Data Availability Statement: Data are available upon reasonable, by the Corresponding Authors.

Conflicts of Interest: The authors declare no conflict of interest.

References

1. Li, X.; Zhao, L.; Yu, X.; Liu, X.; Zhang, X.; Liu, H.; Zhou, W. Water Splitting: From electrode to green energy system. *Nano Micro Lett.* **2020**, *12*, 131. [CrossRef] [PubMed]
2. Li, S.; Li, E.; An, X.; Hao, X.; Jiang, Z.; Guan, G. Transition metal-based catalysts for electrochemical water splitting at high current density: Current status and perspectives. *Nanoscale* **2021**, *13*, 12788. [CrossRef] [PubMed]
3. Jana, J.; Thi Ngo, Y.L.; Chung, J.S.; Huan Hur, H. Contribution of carbon dot nanoparticles in electrocatalysis: Development in energy conversion process. *J. Electrochem. Sci. Technol.* **2020**, *11*, 220–237. [CrossRef]
4. Ji, Q.; Zou, L.; Liu, H.; Yong, J.; Chen, J.; Song, Z.; Gao, J. Bimetallic nanoparticles embedded in N-doped carbon nanotubes derived from metal-organic frameworks as efficient electrocatalysts for oxygen evolution reaction. *J. Solid State Chem.* **2021**, *303*, 122515. [CrossRef]
5. Lin, Z.J.; Lü, J.; Hong, M.; Cao, R. Metal–organic frameworks based on flexible ligands (FL-MOFs): Structures and applications. *Chem. Soc. Rev.* **2014**, *43*, 5867–5895. [CrossRef]
6. Wen, Y.; Zhang, P.; Sharma, V.K.; Ma, X.; Zhou, H.C. Metal-organic frameworks for environmental applications. *Cell Rep. Phys. Sci.* **2021**, *2*, 100348. [CrossRef]
7. Wang, H.; Zhu, Q.L.; Zou, R.; Xu, Q. Metal-organic frameworks for energy applications. *Chem* **2017**, *2*, 52–80. [CrossRef]
8. Cheng, Y.; Xiao, X.; Guo, X.; Yao, H.; Pang, H. Synthesis of "Quasi-Ce-MOF" electrocatalysts for enhanced urea oxidation reaction performance. *ACS Sustain. Chem. Eng.* **2020**, *8*, 8675–8680. [CrossRef]
9. Kumar, V.; Kumar, S.; Kim, H.K.; Tsang, D.C.W.; Lee, S.S. Metal organic frameworks as potent treatment media for odorants and volatiles. *Environ. Res.* **2019**, *168*, 336–356. [CrossRef]
10. Xu, G.; Zhu, C.; Gao, G. Recent progress of advanced conductive metal–organic frameworks: Precise synthesis, electrochemical energy storage applications, and future challenges. *Small* **2022**, *18*, 2203140. [CrossRef]
11. Wu, H.B.; Lou, X.W. Metal-organic frameworks and their derived materials for electrochemical energy storage and conversion: Promises and challenges. *Sci. Adv.* **2017**, *3*, eaap9252. [CrossRef]
12. Li, W.; Xiong, D.; Gao, X.; Liu, L. The oxygen evolution reaction enabled by transition metal phosphide and chalcogenide pre-catalysts with dynamic changes. *Chem. Commun.* **2019**, *55*, 8744–8763. [CrossRef]
13. Wan, K.; Luo, J.; Zhou, C.; Zhang, T.; Arbiol, J.; Lu, X.; Mao, B.W.; Zhang, X.; Fransaer, J. Hierarchical porous Ni_3S_4 with enriched high-valence Ni sites as a robust electrocatalyst for efficient oxygen evolution reaction. *Adv. Funct. Mater.* **2019**, *29*, 1900315. [CrossRef]
14. Wan, K.; Luo, J.; Zhang, X.; Subramanian, P.; Fransaer, J. Sulfur-modified nickel selenide as an efficient electrocatalyst for the oxygen evolution reaction. *J. Energy Chem.* **2021**, *62*, 198–203. [CrossRef]
15. Li, P.; Chen, R.; Tian, S.; Xiong, Y. Efficient oxygen evolution catalysis triggered by nickel phosphide nanoparticles compositing with reduced graphene oxide with controlled architecture. *ACS Sustain. Chem. Eng.* **2019**, *7*, 9566–9573. [CrossRef]
16. Sing, C.; Mukhopadhyay, S.; Hod, I. Metal–organic framework derived nanomaterials for electrocatalysis: Recent developments for CO_2 and N_2 reduction. *Nano Converg.* **2021**, *8*, 1. [CrossRef]
17. Tan, X.; Wu, Y.; Lin, X.; Zeb, A.; Xu, X.; Luo, Y.; Liu, J. Application of MOF-derived transition metal oxides and composites as anodes for lithium-ion batteries. *Inorg. Chem. Front.* **2020**, *7*, 4939–4955. [CrossRef]
18. Qin, X.; Kim, D.; Piao, Y. Metal-organic frameworks-derived novel nanostructured electrocatalysts for oxygen evolution reaction. *Carbon Energy* **2021**, *3*, 66–100. [CrossRef]
19. Ullah, N.; Ullah, S.; Khan, S.; Guziejewski, D.; Mirceski, V. A review: Metal-organic framework based electrocatalysts for methanol electro-oxidation reaction. *Int. J. Hydrogen Energy* **2023**, *48*, 3340–3354. [CrossRef]
20. Tran, T.Q.N.; Park, B.J.; Yun, W.H.; Duong, T.N.; Yoon, H.H. Metal–organic framework–derived Ni@C and NiO@C as anode catalysts for urea fuel cells. *Sci. Rep.* **2020**, *10*, 278. [CrossRef]
21. Song, Z.; Cheng, N.; Lushington, A.; Sun, X. Recent progress on MOF-derived nanomaterials as advanced electrocatalysts in fuel cells. *Catalysts* **2016**, *6*, 116. [CrossRef]
22. Han, C.; Zhu, X.; Ding, J.; Miao, T.; Huang, S.; Qian, J. MOF-derived Pt/ZrO_2 carbon electrocatalyst for efficient hydrogen evolution. *Inorg. Chem.* **2022**, *61*, 18350–18354. [CrossRef] [PubMed]
23. Gao, H.; Yang, M.; Du, Z.; Liu, X.; Dai, X.; Lin, K.; Bao, X.Q.; Li, H.; Xiong, D. Metal–organic framework derived bimetal oxide $CuCoO_2$ as efficient electrocatalyst for the oxygen evolution reaction. *Dalton Trans.* **2022**, *51*, 5997–6006. [CrossRef] [PubMed]

24. Majumdar, D.; Roy, S. Development of low-ppm CO sensors using pristine CeO_2 nanospheres with high surface area. *ACS Omega* **2018**, *3*, 4433–4440. [CrossRef]
25. Song, X.Z.; Zhu, W.Y.; Wang, X.F.; Tan, Z. Recent advances of CeO_2-based electrocatalysts for oxygen and hydrogen evolution as well as nitrogen reduction. *ChemElectroChem* **2021**, *8*, 996–1020. [CrossRef]
26. Rohini, B.S.; Nagabhushana, H.; Darshan, G.P.; Basavaraj, R.B.; Sharma, S.C.; Sudarmani, R. Fabricated CeO_2 nanopowders as a novel sensing platform for advanced forensic, electrochemical and photocatalytic applications. *Appl. Nanosci.* **2017**, *7*, 815–833. [CrossRef]
27. Xie, W.; Liu, B.; Xiao, S.; Li, H.; Wang, Y.; Cai, D.; Wang, D.; Wang, L.; Liu, Y.; Li, Q.; et al. High performance humidity sensors based on CeO_2 nanoparticles. *Sens. Actuators B* **2015**, *215*, 125–132. [CrossRef]
28. Tamizhdurai, P.; Sakthinathan, S.; Chen, S.M.; Shanthi, K.; Sivasanker, S.; Sangeetha, P. Environmentally friendly synthesis of CeO_2 nanoparticles for the catalytic oxidation of benzyl alcohol to benzaldehyde and selective detection of nitrite. *Sci. Rep.* **2017**, *7*, 46372. [CrossRef]
29. Maheswari, N.; Muralidharan, G. Hexagonal CeO_2 nanostructures: An efficient electrode material for supercapacitors. *Dalton Trans.* **2016**, *45*, 14352–14362. [CrossRef]
30. Charbgoo, F.; Ahmad, M.B.; Darroudi, M. Cerium oxide nanoparticles: Green synthesis and biological applications. *Int. J. Nanomed.* **2017**, *12*, 1401–1413. [CrossRef]
31. Sridharan, M.; Maiyalagan, T.; Panomsuwan, G.; Techapiesancharoenkij, R. Enhanced electrocatalytic activity of cobalt-doped ceria embedded on nitrogen, sulfur-doped reduced graphene oxide as an electrocatalyst for oxygen reduction reaction. *Catalysts* **2022**, *12*, 6. [CrossRef]
32. Siddeeg, S.M. A novel synthesis of TiO_2/GO nanocomposite for the uptake of Pb^{2+} and Cd^{2+} from wastewater. *Mater. Res. Exp.* **2020**, *7*, 025038. [CrossRef]
33. Huang, L.; Yang, H.; Zhang, Y.; Xiao, W. Study on synthesis and antibacterial properties of Ag NPs/GO nanocomposites. *J. Nanomater.* **2016**, *2016*, 5685967. [CrossRef]
34. Shahriari, S.; Sastry, M.; Panjikar, S.; Singh Raman, R.K. Graphene and graphene oxide as a support for biomolecules in the development of biosensors. *Nanotechnol. Sci. Appl.* **2021**, *14*, 197–220. [CrossRef]
35. Yu, Y.; Li, Y.; Pan, Y.; Liu, C.J. Fabrication of palladium/graphene oxide composite by plasma reduction at room temperature. *Nanoscale Res. Lett.* **2012**, *7*, 234. [CrossRef]
36. Czepa, W.; Pakulski, D.; Witomska, S.; Patroniak, V.; Ciesielski, A.; Samorí, P. Graphene oxide-mesoporous SiO_2 hybrid composite for fast and efficient removal of organic cationic contaminants. *Carbon* **2020**, *158*, 193–201. [CrossRef]
37. Azimi, F.; Nabizadeh, R.; Hassanvand, M.S.; Rastkari, N.; Nazmara, S.; Naddafi, K. Photochemical degradation of toluene in gas-phase under UV/visible light graphene oxide –TiO_2 nanocomposite: Influential operating factors, optimization, and modeling. *J. Environ. Health Sci. Eng.* **2019**, *17*, 671–683. [CrossRef]
38. Lei, M.; Wang, Z.B.; Li, J.S.; Tang, H.L.; Liu, W.J.; Wang, Y.G. CeO_2 nanocubes-graphene oxide as durable and highly active catalyst support for proton exchange membrane fuel cell. *Sci. Rep.* **2014**, *4*, 7415. [CrossRef]
39. Simon, R.; Chakraborty, S.; Darshini, K.S.; Mary, N.L. Electrolyte dependent performance of graphene–mixed metal oxide composites for enhanced supercapacitor applications. *SN Appl. Sci.* **2020**, *2*, 1898. [CrossRef]
40. Chen, Y.; Huang, N.; Liang, Y. Preparation of CeO_2/Cu-MOF /GO composite for efficient electrocatalytic oxygen evolution reaction. *Ionics* **2021**, *27*, 4347–4360. [CrossRef]
41. Makhafola, M.D.; Modibane, K.D.; Ramohlola, K.E.; Maponya, T.C.; Hata, M.J.; Makgopa, K.; Iwuoha, E.I. Palladinized graphene oxide-MOF induced coupling of Volmer and Heyrovsky mechanisms, for the amplifcation of the electrocatalytic efficiency of hydrogen evolution reaction. *Sci. Rep.* **2021**, *11*, 17219. [CrossRef] [PubMed]
42. Xiao, Y.; Guo, B.; Zhang, J.; Hu, C.; Ma, R.; Wang, D.; Wang, J. A bimetallic MOF@graphene oxide composite as an efficient bifunctional oxygen electrocatalyst for rechargeable Zn–air batteries. *Dalton Trans.* **2020**, *49*, 5730–5735. [CrossRef]
43. Malik, W.M.A.; Afaq, S.; Mahmood, A.; Niu, L.; Yousaf ur Rehman, M.; Ibrahim, M.; Mohyuddin, A.; Qureshi, A.M.; Ashiq, M.N.; Chughtai, A.H. A facile synthesis of CeO_2 from the GO@Ce-MOF precursor and its efficient performance in the oxygen evolution reaction. *Front. Chem.* **2022**, *10*, 996560. [CrossRef]
44. Deng, D.; Chen, N.; Xiao, X.; Du, S.; Wang, Y. Electrochemical performance of CeO_2 nanoparticle-decorated graphene oxide as an electrode material for supercapacitor. *Ionics* **2017**, *23*, 121–129. [CrossRef]
45. Kasinath, L.; Byrappa, K. Ceria Boosting on In Situ Nitrogen-Doped Graphene Oxide for Efficient Bifunctional ORR/OER Activity. *Front. Chem.* **2022**, *10*, 889579. [CrossRef] [PubMed]
46. Li, S.; Wang, R.; Xie, M.; Xu, Y.; Chen, J.; Jiao, Y. Construction of trifunctional electrode material based on Pt-Coordinated Ce-based metal organic framework. *J. Colloid Interface Sci.* **2022**, *622*, 378–389. [CrossRef] [PubMed]
47. Sun, W.; Li, X.; Sun, C.; Huang, Z.; Xu, H.; Shen, W. Insights into the pyrolysis processes of Ce-MOFs for preparing highly active catalysts of toluene combustion. *Catalysts* **2019**, *9*, 682. [CrossRef]
48. Kumar, E.; Selvarajan, P.; Balasubramanian, K. Preparation and studies of cerium dioxide(CeO_2) nanoparticles by microwave-assisted solution method. *Recent Res. Sci. Technol.* **2010**, *2*, 37–41.
49. Tiwary, C.S.; Sarkar, R.; Kumbhakar, P.; Mitra, A.K. Synthesis and optical characterization of monodispersed Mn2+ doped CdS nanoparticles. *Phys. Lett. A* **2008**, *372*, 5825–5830. [CrossRef]

50. Smirnov, A.; Pinargote, N.W.S.; Peretyagin, N.; Pristinskiy, P.; Peretyagin, P.; Bartolomé, J.F. Zirconia reduced graphene oxide nano-hybrid structure fabricated by the hydrothermal reaction method. *Materials* **2020**, *13*, 687. [CrossRef]
51. Quach, Q.; Abdel-Fattah, T.M. Silver nanoparticles functionalized nanosilica grown over graphene oxide for enhancing antibacterial effect. *Nanomaterials* **2022**, *12*, 3341. [CrossRef]
52. Zhang, K.; Suh, J.M.; Lee, T.H.; Cha, J.H.; Choi, J.W.; Jang, H.W.; Varma, R.S.; Shokouhimehr, M. Copper oxide–graphene oxide nanocomposite: Efficient catalyst for hydrogenation of nitroaromatics in water. *Nano Conv.* **2019**, *6*, 6. [CrossRef]
53. Andrijantho, E.; Shoelarta, S.; Subiyanto, G.; Rifki, S. Facile synthesis of graphene from graphite using ascorbic acid as reducing agent. *AIP Conf. Proc.* **2016**, *1725*, 020003.
54. Chibac-scutaru, A.L.; Podasca, V.; Dascalu, J.A.; Melinte, V. Exploring the influence of synthesis parameters on the optical properties for various CeO_2 NPs. *Nanomaterials* **2022**, *12*, 1402. [CrossRef]
55. Dezfuli, A.S.; Ganjali, M.R.; Naderi, H.R.; Norouzi, P. A high performance supercapacitor based on a ceria/graphene nanocomposite synthesized by a facile sonochemical method. *RSC Adv.* **2015**, *5*, 46050–46058. [CrossRef]
56. Sisubalan, N.; Karthikeyan, C.; Kumar, V.S.; Varaprasad, K.; Hameed, A.S.H.; Vanajothi, R.; Sadiku, R. Biocidal activity of Ba^{2+}-doped CeO_2 NPs against *Streptococcus mutans* and *Staphylococcus aureus* bacterial strains. *RSC Adv.* **2021**, *11*, 30623–30634. [CrossRef]
57. Wang, N.; Wang, S.; Yang, J.; Xiao, P.; Zhu, J. Promotion effect of Ce doping on catalytic performance of $LaMnO_3$ for CO oxidation. *Catalysts* **2022**, *12*, 1409. [CrossRef]
58. Chen, Z.; Yang, M.; Li, Z.; Liao, W.; Chen, B.; Yang, T.; Hu, R.; Yang, Y.; Meng, S. Highly sensitive and convenient aptasensor based on Au NPs@Ce-TpBpy COF for quantitative determination of zearalenone. *RSC Adv.* **2022**, *12*, 17312. [CrossRef]
59. Guo, Z.; Zhao, X.; Chen, G.; Zhao, W.; Liu, T.; Hu, R.; Jiang, X. Controllable synthesis of magic cube-like Ce-MOF-derived Pt/CeO_2 catalysts for formaldehyde oxidation. *Nanoscale* **2022**, *14*, 12713–12721. [CrossRef]
60. Jiao, Z.; Zhou, G.; Zhang, H.; Shen, Y.; Zhang, X.; Li, J.; Gao, X. Effect of calcination temperature on catalytic performance of CeCu oxide in removal of quinoline by wet hydrogen peroxide oxidation from water. *J. Braz. Chem. Soc.* **2018**, *29*, 2233–2243. [CrossRef]
61. Fu, Z.; Qi, P.; Liu, H.; Zhang, Q.; Zhao, Y.; Feng, X. Influence of oxidative properties of Ce_xZr_{1-x} O_2 catalyst on partial oxidation of dimethyl ether. *Catalysts* **2022**, *12*, 1536.
62. Taratayko, A.; Kolobova, E.; Mamontov, G. Graphene oxide decorated with Ag and CeO_2 nanoparticles as a catalyst for room-temperature 4-nitrophenol reduction. *Catalysts* **2022**, *12*, 1393. [CrossRef]
63. Zhao, F.; Wang, L.; Zhao, L.; Qu, l.; Dai, L. Graphene oxide nanoribbon assembly toward moisture powered information storage. *Adv. Mater.* **2017**, *29*, 1604972. [CrossRef] [PubMed]
64. Hanifah, M.F.R.; Jaffar, J.; Othman, M.H.; Ismail, A.F.; Rahman, M.A.; Yusof, N.; Aziz, F.; Salleh, W.N.W.; Ilbeygi, H. Electrocatalytic performance impact of various bimetallic Pt-Pd alloy atomic ratio in robust ternary nanocomposite electroccatalyst toward boosting of methanol electrooxidation reaction. *Electrochim. Acta* **2022**, *403*, 139608. [CrossRef]
65. Kohantorabi, M.; Gholami, M.R. MxNi100x (M = Ag, and Co) nanoparticles supported on CeO_2 nanorods derived from Ce–metal organic frameworks as an effective catalyst for reduction of organic pollutants: Langmuir–Hinshelwood kinetics and mechanism. *New J. Chem.* **2017**, *41*, 10948–10958. [CrossRef]
66. Ye, J.; Cheng, D.G.; Chen, F.; Zhan, X. Metal-organic framework-derived CeO_2 nanosheets confining ultrasmall Pd nanoclusters catalysts with high catalytic activity. *Int. J. Hydrogen Energy* **2021**, *46*, 39892–39902. [CrossRef]
67. Afza, N.; Shivakumar, M.S.; Alam, M.W.; Kumar, A.N.; Bhatt, A.S.; Murthy, H.C.A.; Ravikumar, C.R.; Mylarappa, M.; Selvanandan, S. Facile hydrothermal synthesis of cerium oxide/rGO nanocomposite for photocatalytic and supercapacitor applications. *Appl. Surf. Sci. Adv.* **2022**, *11*, 100307. [CrossRef]
68. Li, T.; Liu, H. A simple synthesis method of nanocrystals CeO_2 modified rGO composites as electrode materials for supercapacitors with long time cycling stability. *Powder Technol.* **2018**, *327*, 275–281. [CrossRef]
69. Pandit, B.; Sankapal, B.R.; Koinkar, P.M. Novel chemical route for CeO_2/MWCNTs composite towards highly bendable solid-state supercapacitor device. *Sci. Rep.* **2019**, *9*, 5892. [CrossRef]
70. Zhou, R.; Li, Y.; Wang, R.; Su, G.; Gao, R.; Cao, L.; Dong, B. Two-phase synthesis of Fe doped cerium phosphate ultra-fine nanocrystals for efficient oxygen evolution. *New J. Chem.* **2022**, *46*, 2609–2617. [CrossRef]
71. Aashima; Uppal, S.; Arora, A.; Gautam, S.; Singh, S.; Choudhary, R.J.; Mehta, S.K. Magnetically retrievable Ce-doped Fe_3O_4 nanoparticles as scaffolds for the removal of azo dyes. *RSC Adv.* **2019**, *9*, 23129–23141. [CrossRef]
72. Nagajyothi, P.C.; Yoo, K.; Eom, I.Y.; Shim, J. $CoFe_2O_4$ NPs supported on graphitic carbon nitride as inexpensive electrocatalysts for methanol oxidation reaction. *Cerami. Int.* **2022**, *48*, 11623–11628. [CrossRef]
73. Demir, E.; Akbayrak, S.; Önal, A.M.; Özkar, S. Ceria supported ruthenium (0) nanoparticles: Highly efficient catalysts in oxygen evolution reaction. *J. Colloid Interface Sci.* **2019**, *534*, 701–704. [CrossRef]
74. Sung, M.C.; Lee, G.H.; Kim, D.W. $CeO_2/Co(OH)_2$ hybrid electrocatalyst for efficient hydrogen and oxygen evolution reaction. *J. Alloys Compd.* **2019**, *800*, 450–455. [CrossRef]
75. Gao, W.; Xia, Z.; Cao, F.; Ho, J.C.; Jiang, Z.; Qu, Y. Comprehensive understanding of the spatial configurations of CeO_2 in NiO for the electrocatalytic oxygen evolution reaction: Embedded or surface-loaded. *Adv. Funct. Mater.* **2018**, *28*, 1706056. [CrossRef]
76. Liu, Y.; Ma, C.; Zhang, Q.; Wang, W.; Pan, P.; Gu, L.; Xu, D.; Bao, J.; Dai, Z. 2D electron gas and oxygen vacancy induced high oxygen evolution performances for advanced Co_3O_4/CeO_2 nanohybrids. *Adv. Mater.* **2019**, *31*, 190006.

77. Kim, J.H.; Shin, K.; Kawashima, K.; Youn, D.H.; Lin, J.; Hong, T.E.; Liu, Y.; Wygant, B.R.; Wang, J.; Henkelman, G.; et al. Enhanced activity promoted by CeOx on a CoOx electrocatalyst for the oxygen evolution reaction. *ACS Catal.* **2018**, *8*, 4257–4265. [CrossRef]
78. Li, T.; Li, S.; Liu, Q.; Tian, Y.; Zhang, Y.; Fu, G.; Tang, Y. Hollow Co_3O_4/CeO_2 heterostructures in situ embedded in N-Doped carbon nanofibers enable outstanding oxygen evolution. *ACS Sustain. Chem. Eng.* **2019**, *7*, 17950–17957. [CrossRef]
79. Kang, Y.; Wang, W.; Li, J.; Mi, Y.; Gong, H.; Lei, Z. 3D *Rosa Centifolia*-like CeO_2 encapsulated with N-doped carbon as an enhanced electrocatalyst for Zn-Air Batteries. *J. Colloid Interface Sci.* **2020**, *578*, 796–804. [CrossRef]
80. Sivanantham, A.; Ganesan, P.; Shanmugam, S. A Synergistic Effect of Co and CeO2 in nitrogen-doped carbon nanostructure for the enhanced oxygen electrode activity and stability. *Appl. Catal. B-Environ.* **2018**, *237*, 1148–1159. [CrossRef]
81. Goswami, C.; Yamada, Y.; Matus, E.V.; Ismagilov, I.Z.; Kerzhentsev, M.; Bharali, P. Elucidating the role of oxide-oxide/carbon interfaces of CuOx-CeO2/C in boosting electrocatalytic performance. *Langmuir* **2020**, *36*, 15141–15152. [CrossRef] [PubMed]